NANO LETTERS

Letter

pubs.acs.org/NanoLett

Atomic-Scale Interfacial Band Mapping across Vertically Phased-Separated Polymer/Fullerene Hybrid Solar Cells

Min-Chuan Shih,[†] Bo-Chao Huang,[†] Chih-Cheng Lin,[‡] Shao-Sian Li,[‡] Hsin-An Chen,[‡] Ya-Ping Chiu,*[,†] and Chun-Wei Chen*[,‡]

[†]Department of Physics, National Sun Yat-sen University, Kaohsiung, 80424, Taiwan

[‡]Department of Materials Science and Engineering, National Taiwan University, Taipei, 10617, Taiwan

Supporting Information

ABSTRACT: Using cross-sectional scanning tunneling microscope (XSTM) with samples cleaved in situ in an ultrahigh vacuum chamber, this study demonstrates the direct visualization of high-resolution interfacial band mapping images across the film thickness in an optimized bulk heterojunction polymer solar cell consisting of nanoscale phase segregated blends of poly(3-hexylthiophene) (P3HT) and [6,6]-phenyl C61 butyric acid methyl ester (PCBM). We were able to achieve the direct observation of the interfacial band alignments at the donor (P3HT)-acceptor (PCBM) interfaces and at the interfaces between the photoactive P3HT:PCBM blends and the poly(3,4-ethylenedioxythiophene) poly(styrenesulfonate) (PEDOT:PSS) anode modification layer with an atomic-scale spatial resolution. The unique advantage of using XSTM to characterize polymer/fullerene bulk heterojunction solar cells allows us to explore simultaneously the quantitative link between the vertical morphologies and their corresponding local electronic properties. This provides an atomic insight of interfacial band alignments between the two opposite electrodes, which will be crucial for improving the efficiencies of the charge generation, transport, and collection and the corresponding device performance of polymer solar cells.

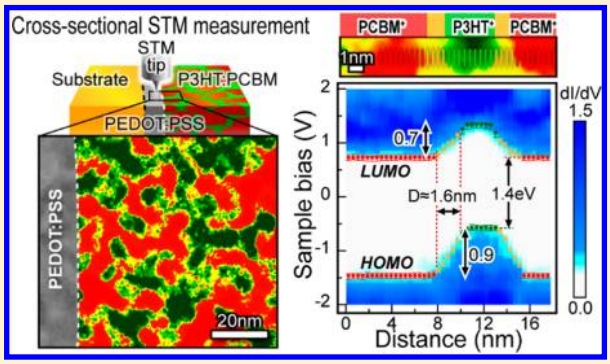

KEYWORDS: *Polymer/fullerene hybrid solar cells, bulk heterojunction, band mapping, interface, scanning tunneling spectroscopy*

Polymer solar cells[1−4] have attracted significant interest in the fabrication of low-cost and mechanically flexible photovoltaic devices in the past decade because they enable solution processing and patterning on flexible substrates. The most intensively studied materials for bulk heterojunction (BHJ) polymer solar cells consist of poly(3-hexylthiophene) (P3HT) and fullerene derivative phenyl-C61-butyric acid methyl ester (PCBM) blends, which have power conversion efficiencies of approximately 4−5%.[4,5] Researchers have recently achieved high photovoltaic efficiencies close to 7−8% by incorporating new small band gap semiconducting polymers.[6] Because of the short exciton diffusion length (<20 nm) of a semiconducting polymer,[7−9] electron acceptors usually mix with polymers at a nanometer-length scale to form BHJs with a nanoscale interpenetrating donor/acceptor network. Neutral bound electron−hole pairs (excitons) represent the dominant photogenerated species in a conventional BHJ polymer solar, and these excitons can be dissociated from Coulomb attraction by offering electrons an energetically favorable pathway from the polymer (donor) to an electron-accepting specie (acceptor). It is concluded that the device performance strongly depends on the optimized phase separated donor−acceptor morphology of the BHJ, which ensures efficient dissociations of photogenerated excitons and continuous pathways for transporting charge carriers to electrodes.[10] The most popular device structure usually consists of a polymer/fullerene blend sandwiched between an PEDOT:PSS-coated indium tin oxide (ITO) anode and a low work function metal cathode.[5] Thus, the interfacial energy band structures at the donor/acceptor interfaces and the photoactive-layer/electrode interfaces have a crucial effect on the efficiency of photoinduced charge separation, transport, and collection and the corresponding device performance. Researchers have used many high-resolution characterization tools, including scanning probe microscopy (SPM)[5,11−20] and transmission electron microscopy (TEM),[18,21,22] to probe the nanoscale morphology of BHJ solar cells. Three-dimensional (3D) electron tomography[22] has recently provided insight into the nanoscale organization of BHJ polymer solar cells, providing the critical morphological parameters of both the lateral and vertical directions of the films. Compared to the TEM technique, the unique advantage of using SPM to characterize BHJ solar cells is that it can explore the quantitative link between nanoscale morphologies and their local electronic properties simultaneously. However, most SPM studies on BHJ

Received: January 8, 2013
Revised: April 23, 2013

   dx.doi.org/10.1021/nl400091f | *Nano Lett.* XXXX, XXX, XXX−XXX

morphology have been conducted on or through the top surface of the film. Because photogenerated carriers must move toward the two opposite electrodes across the film thickness rather than parallel to the film surface, an understanding of the correlation between the cross-sectional nanoscale morphology and the local electronic structures of BHJ materials in the vertical direction is of crucial importance for further improving device performance. Because scanning tunneling microscope (STM) combined with scanning tunneling spectroscopy (STS) measurements can provide spatially resolved tunneling spectroscopy and the local density of states (LDOS) information of the organic samples simultaneously, this study demonstrates the interfacial band mapping images of an optimized P3HT:PCBM bulk heterojunction solar cell using cross-sectional scanning tunneling microscope (XSTM) with samples cleaved in situ in an ultrahigh vacuum (UHV) chamber. The results allow us to visualize the vertically phase-separated BHJ morphology of a P3HT:PCBM hybrid solar cell device at a subnanometer resolution. Most importantly, this method enables the direct observation of the interfacial band alignments at the donor−acceptor interfaces and the interfaces between the P3HT:PCBM blends and PEDOT:PSS layer with atomic-scale spatial resolution. This type of analysis reveals the interplay between the vertical phase-segregated nanomorphology and local interfacial electronic structures of the polymer/fullerene bulk heterojunctions, which are crucial for improving the efficiencies of charge generation, transport, and collection of polymer solar cell devices.

To obtain high-quality cross-sectional polymer/fullerene hybrid samples, a Si(100) wafer was selected as the supporting substrate because it exhibits an excellent cleaved surface in previous XSTM measurements.[23−26] For device fabrication, a 30 nm thick layer of PEDOT:PSS (Baytron P 4083) was first spun-cast onto the Si(100) substrate. After baking the PEDOT:PSS films at 120 °C for 1 h, the devices were moved into a nitrogen-purged glove box for subsequent deposition. The photoactive layer was deposited on top of the PEDOT:PSS layer by spin coating using a 1:0.8 weight ratio blend of P3HT:PCBM dissolved in chlorobenzene. The photoactive layer was approximately 100 nm thick. The device was thermally annealed at 150 °C for 5 min in the nitrogen glove box. Next, in our STM studies, experiments were all performed in an UHV chamber with base pressure of approximately 5×10^{-11} Torr. A common thickness of the sample (∼0.5 mm) was used in our experiments. Before loading the sample into the UHV chamber, a notch across the sample of a ∼0.3 mm length at the middle position was suitably prepared on the organic film side.[27] The sample was then transferred to an UHV chamber and cleaved in situ at room temperature to obtain the cross-sectional slice of the Si/PEDOT:PSS/P3HT:PCBM film as shown schematically in Figure 1a,b, respectively. Such an approach may avoid possible surface contamination of the films.[28] The chamber was equipped with a variable temperature STM, which is able to perform STS measurements. The tunneling spectra were acquired by using the current imaging tunneling spectroscopy (CITS) mode, where a series of tunnel current images was obtained at different sample bias voltage V_s. In this work, V_s was varied from +4.0 to −4.0 V for STS measurements. STM and STS images were simultaneously acquired at temperature of ∼100 K. STM combined with STS can provide relevant information directly on the local electronic structure at interfaces of PCBM:P3HT/PEDOT:PSS. Figure 1c shows the

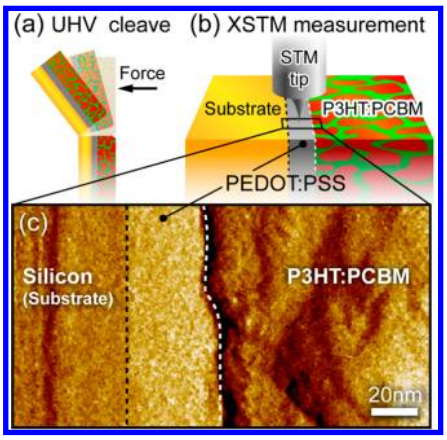

Figure 1. (a) Schematic illustration of the cleaving sample procedure in XSTM measurements. (b) Schematic description of XSTM measurements. (c) Typical cross-sectional STM topography image of the Si/PEDOT:PSS/P3HT:PCBM film. The image was taken at a sample bias of +4 V and tunneling current of 150 pA.

typical XSTM topography image of the P3HT:PCBM hybrid film on PEDOT:PSS/Si(100) substrate at a sample bias of +4.0 V. Three different regions with distinct interfaces at P3HT:PCBM/PEDOT:PSS and PEDOT:PSS/Si can be clearly revealed from the specifically electronic characteristics of the substrate Si, PEDOT:PSS, and P3HT:PCBM blend film as shown in Figure 2a−d. The position of the zero sample bias in

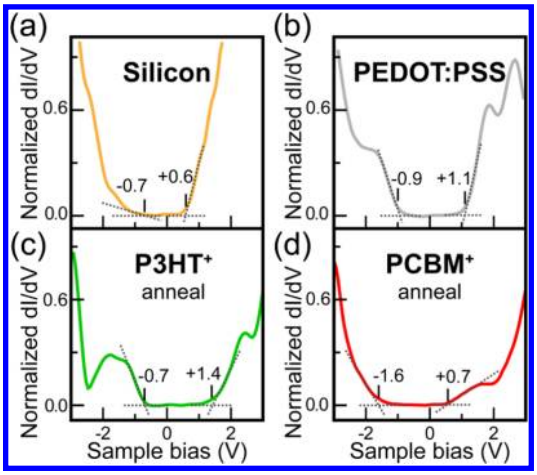

Figure 2. Specifically normalized dI/dV curves of (a) silicon (Si), (b) PEDOT:PSS, (c) P3HT-rich ($P3HT^+$), and (d) PCBM-rich ($PCBM^+$) region of the thermally annealed sample, respectively. The current onsets in filled and empty states were indicated each by dark ticks.

the STM measurements indicates the Fermi level of the system. The current onsets in the occupied/unoccupied states, which correspond to valence and conduction bands (VB/CB) or (highest occupied molecular orbitals/lowest unoccupied molecular orbitals (HOMO/LUMO)) edges, are extracted and indicated by tick marks following the methodology developed in ref 29. (also see the Supporting Information Figure 1). The precision of the onset energy determined by this method was estimated to be ±0.10 eV in this study. A very sharp identification at the boundary between Si and PEDOT:PSS can be clearly distinguished due to their specific individual tunneling spectroscopy characteristics (Figure 2a,b). In addition, two types of dI/dV curves appear in the

dx.doi.org/10.1021/nl400091f | Nano Lett. XXXX, XXX, XXX−XXX

P3HT:PCBM hybrid region. One curve demonstrates a hole-conducting (p-type) semiconductor behavior with the specific LUMO and HOMO levels located at +1.4 and −0.7 V, respectively (Figure 2c). This type of curve resembles the typical (dI/dV) curve obtained from the pristine P3HT (Supporting Information Figure 2). The other dI/dV spectrum has the specific onset bias of LUMO and HOMO levels located at +0.7 and −1.6 V (Figure 2d), showing the typical characteristics of an electron-conducting (n-type) semiconductor. This type of curve primarily results from the contribution of PCBM (Supporting Information Figure 2). Referring to electronically specific tunneling spectra of these materials, XSTM measurements with a subnanometer resolution in the vertical direction of the polymer/fullerene BHJ solar cell device make it possible to investigate the interfacial electronic properties of the donors (P3HT) and acceptors (PCBM) and those at the interfaces between the P3HT:PCBM hybrid blends and the PEDOT:PSS layer.

Figure 3a,c shows the XSTM topography images of the P3HT:PCBM hybrid films without and with the post-thermal

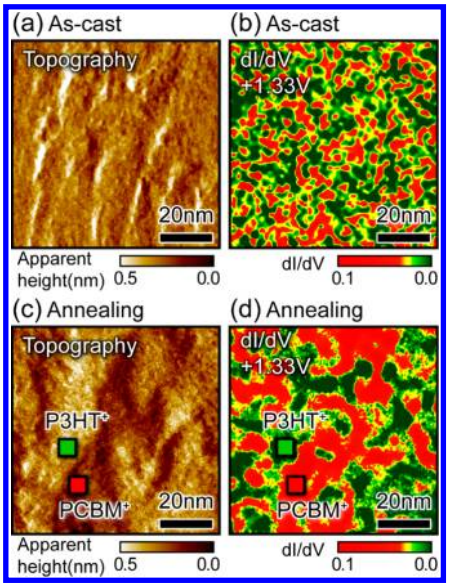

Figure 3. Cross-sectional STM topography images of (a) the as-cast and (c) the thermally annealed P3HT:PCBM sample. Normalized dI/dV images probed at +1.33 V sample bias of (b) the as-cast and (d) the thermally annealed P3HT:PCBM sample. The regions colored by green and red in the dI/dV images are electronically identified and represented as the portions of $P3HT^+$ and $PCBM^+$, respectively.

annealing treatment. The post-thermal annealed sample shows a more phase-separated morphology than the as-cast sample with the more recognizable P3HT-dominant and PCBM-dominant regions. Mappings of the corresponding tunneling conductance were recorded simultaneously with topographical images by acquiring the differential tunneling current (dI/dV) characteristics as a function of the sample bias (Figure 3b,d). The dI/dV spectrum of PCBM exhibits the typical characteristics of an electron-conducting (n-type) semiconductor. Thus, the regions with higher tunneling current recorded at +1.33 V sample bias, which is below the characteristic current onset of P3HT at positive sample bias, are primarily associated with the contribution of PCBM. These two regions can be clearly identified by their differential electronic characteristics (Supporting Information Figure 3). The red areas in Figure 3b,d represent the PCBM-rich ($PCBM^+$) regions, whereas the green areas represent the P3HT-rich ($P3HT^+$) regions. The PCBM molecules in the as-cast P3HT:PCBM hybrid sample are more uniformly distributed within the P3HT matrix with a smaller domain size of approximately 2−4 nm. Post-thermal treatment causes the PCBM molecules to aggregate, forming larger clusters with a domain width of approximately 10−20 nm. These domains tend to form an interpenetrated network within the P3HT matrix along the vertical direction, providing the pathways required for charge transport. This result is also consistent with a larger current density and a higher power conversion efficiency of ∼4.2% in the annealed device compared to the as-cast sample of ∼2.4% (see Supporting Information Figure 4). Also, the morphological results obtained from the XSTM measurement show excellent agreement with the observation of the cross-sectional TEM images.[30,31] These results suggest that the XSTM can be a unique tool to simultaneously probe the vertical nanoscale morphology and locally corresponding electronic properties of P3HT:PCBM BHJs across the film thickness at a subnanometer resolution (Supporting Information Figure 5). It is worth noting that the degree of the fullerene aggregation will result in some fluctuation in electronic behaviors and the corresponding energy levels in the P3HT:PCBM samples.

Figure 4a−d shows the analysis of interfacial electronic band mapping using spatial spectroscopic measurements through the

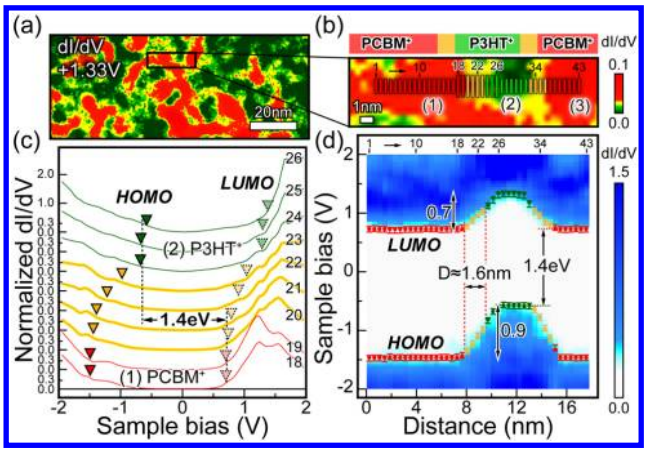

Figure 4. (a) Normalized dI/dV images of the P3HT:PCBM active layer with the thermal annealing treatment. (b) A magnified sliced image across the $PCBM^+(1)/(P3HT^+)(2)/PCBM^+(3)$ heterojunction. (c) Local density of states (LDOS) measurements from $PCBM^+$ to $P3HT^+$ across the interfacial region are indicated by red, green, and yellow curves. (d) Atomic-scale evolution of band alignment across the $P3HT^+/PCBM^+$ heterointerface. Scientific position numbering is made in panel b, and the corresponding numbers by the electronic curves in panel c, and above the band structure in panel d are also indicated.

P3HT and PCBM heterojunctions. Figure 4a shows the normalized dI/dV images of the P3HT:PCBM active layer with the thermal annealing treatment, while a sliced image across the $PCBM^+/P3HT^+/PCBM^+$ heterojunction is magnified in Figure 4b. The areas numbered (1) and (3) in Figure 4b represent the $PCBM^+$ domains, whereas the area numbered (2) is the $P3HT^+$ domain. To investigate the subnanometer electronic properties, the colored solid bars of Figure 4b indicate the scanning profile positions with a spatial separation of 0.4 nm across the regions numbered from (1) to (3). Figure 4c shows some representative tunneling spectra acquired across

dx.doi.org/10.1021/nl400091f | Nano Lett. XXXX, XXX, XXX−XXX

the P3HT:PCBM heterojunction with the differential tunneling current dI/dV as a function of the sample bias. The approximate locations of HOMO and LUMO levels, which result from the offsets of the tunneling current in filled and empty states, are extracted and indicated by solid and dashed triangle marks in Figure 4c. On the basis of the electronic characteristics of these spatial spectroscopic measurements, Figure 4d shows the XSTM mapping image of LDOS and the band alignment across the heterointerfaces of PCBM$^+$/P3HT$^+$/PCBM$^+$ at a spatial resolution of 0.4 nm. The offsets of the HOMO and LUMO levels for P3HT and PCBM are those of a typical type II heterojunction. The offset in the LUMO level between P3HT and PCBM is approximately 0.7 eV, which is larger than the typical binding energy of excitons in polymer (~0.2−0.5 eV).[32,33] This suggests that charge separation may occur at the interface with electron transfer from P3HT to PCBM. The offset in the HOMO levels between P3HT and PCBM is approximately 0.9 eV. The energy difference between the HOMO level of P3HT and the LUMO level of PCBM, which is usually related to the open circuit voltage of a donor−acceptor BHJ solar cell,[34] is estimated to be approximately 1.4 eV. The atomic-scale resolution band energy diagram at the P3HT/PCBM heterojunction based on the XSTM measurement shows a consistent trend with the values reported in previous studies which measured the bulk active layer films by comparing the ionization potential or electron affinity of the active layer components.[35] Most importantly, the atomic-scale evolution of the local electronic structure across the P3HT/PCBM interface makes it possible to directly visualize the distinct band bending characteristics and electronic configurations at the interface. The lateral extension (D) at the interface between the P3HT and PCBM domains has an estimated width of 1.6 nm. Because the typical diffusion length of excitons in conjugated polymer is approximately 10 nm,[9] the mean domain width of P3HT within 10−20 nm (Figure 3d) suggests that excitons can reach these interfaces during their lifetime. Accordingly, the large potential gradient developing at the P3HT/PCBM interface leads to efficient charge separation of photogenerated excitons into free electrons or holes. This in turn may account for the ultrafast electron transfer for the polymer/fullerene heterojunction interface.[36] In addition, the normalized dI/dV curve at the interfacial region between the PCBM$^+$ and P3HT$^+$ domains has the position of the LUMO level close to the Fermi level, suggesting an *n*-type electronic characteristic at the interface. The electronic configurations and LDOS at the interfacial region are closer to those at the PCBM$^+$ region than at the P3HT$^+$ region (Supporting Information Figure 6), implying that electron transporting might be more efficient than hole transport at the interfacial region.[37] Previous research has also proposed that there would be more significant charge transfer through interfacial bridge states from the excited state of P3HT to the ground state of fullerene atoms when the photoactive layer is under illumination.[38] Thus, it would be expected that more distinct n-type transporting of carriers through these interfacial states would be observed as the P3HT:PCBM blend film is under illumination at an operating device. However, it is still not clear whether these interfacial states are responsible for the filamentary transport in polymer solar cells with current confinement in nanodomains[10,39] as a consequence of energetic disorder in the donor/acceptor blend film. The subnanometer resolution measurement of local current distributions of a BHJ solar cell device under illumination will be performed in our next project to explore the physics of microscopic carrier generation and transport using the cross-sectional STM technique as developed here.

In addition to the band mapping across the heterointerfaces of P3HT and PCBM, the energy level alignment at the interfaces between the photoactive layer of P3HT:PCBM hybrids and the interfacial anode modification layer of PEDOT:PSS has also generated immense interest because of the crucial roles these materials play in charge transport and collection. The uniqueness of cross-sectional STM measurements makes it possible to explore the interfacial electronic structures between PEDOT:PSS and P3HT:PCBM hybrid layers, which cannot be usually done using the conventional SPM in the lateral direction. Figure 5a shows the normalized

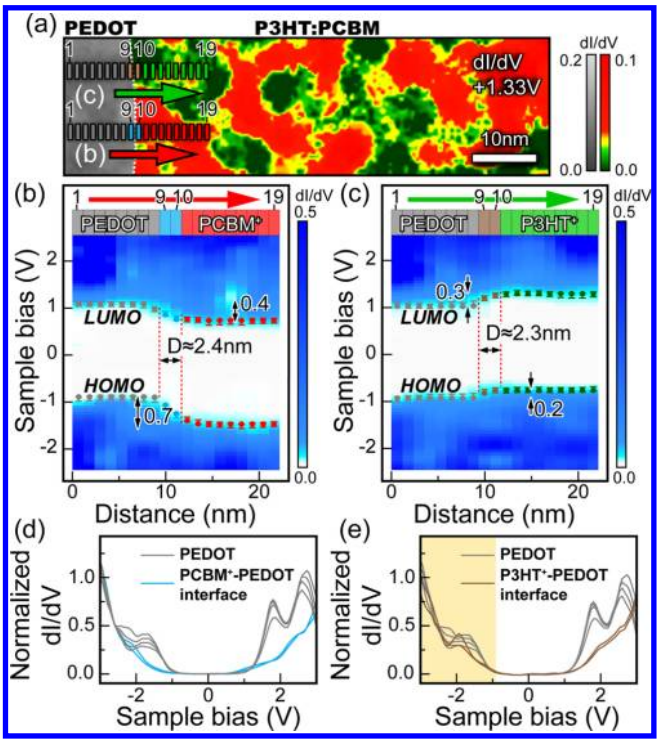

Figure 5. (a) Normalized dI/dV images of the PEDOT:PSS and P3HT:PCBM active layer. The corresponding band alignments across the red arrow (PEDOT:PSS/PCBM$^+$) and the green arrow (PEDOT:PSS/P3HT$^+$) heterointerfaces in (a) are mapped in (b) and (c), respectively. Comparisons of LDOS between the PEDOT:PSS layer and the interfacial regions consisting of (d) PEDOT:PSS/PCBM$^+$ and (e) PEDOT:PSS/P3HT$^+$. Scientific position numbering is made in panel a, and the corresponding numbers above the band structure in panel b and in panel c are also indicated. The numbers 9 and 10 represented the position of the interface of PEDOT:PSS/P3HT$^+$ and PEDOT:PSS/PCBM$^+$.

(dI/dV) images obtained at +1.33 V, in which the interface between PEDOT:PSS and P3HT:PCBM hybrid was marked by the white dash line. The green and red arrows indicate the positions of the spectroscopy measurements scanned across the PEDOT:PSS/P3HT$^+$ or PEDOT:PSS/PCBM$^+$ interfaces, respectively. Figure 5b,c shows the corresponding band mapping images at the PEDOT:PSS/PCBM$^+$ and PEDOT:PSS/P3HT$^+$ interfaces. Both the LUMO and HOMO energy levels of PEDOT:PSS are higher than those of PCBM molecules and the corresponding LUMO and HOMO energy band offsets at the PEDOT:PSS/PCBM$^+$ interface are

dx.doi.org/10.1021/nl400091f | *Nano Lett.* XXXX, XXX, XXX−XXX

approximately 0.4 and 0.7 eV, respectively, with an estimated interfacial width of approximately 2.4 nm. In contrast, the LUMO and HOMO energy levels of PEDOT:PSS are slightly lower than those of P3HT and the corresponding energy band offsets at the PEDOT:PSS/P3HT$^+$ interface are approximately 0.3 eV for the LUMO level and 0.2 eV for the HOMO level with an estimated interfacial width of approximately 2.3 nm. The corresponding tunneling spectra with respect to the evolution of band alignments across these interfaces are shown in the Supporting Information Figure 7. To understand the local electronic configurations at the PEDOT:PSS/PCBM$^+$ or PEDOT:PSS/P3HT$^+$ interfaces, Figure 5d,e shows the comparison of the normalized dI/dV curves obtained from the PEDOT:PSS layer and these interface regions. The dI/dV curve at PCBM$^+$/PEDOT:PSS interface shows an n-type characteristic when the LUMO level is closer to the Fermi level. A significant difference in LDOS between the PEDOT:PSS and PCBM$^+$/PEDOT:PSS interface regions suggests that electron transport through the PCBM$^+$/PEDOT:PSS interface to the PEDOT:PSS layer may be ineffective. In contrast, the dI/dV curve at the P3HT$^+$/PEDOT:PSS interface demonstrates a p-type characteristic with its HOMO level located closer to the Fermi level. The overlaps in LDOS below the Fermi levels of PEDOT:PSS and P3HT$^+$/PEDOT:PSS interface are significant, suggesting that hole transport through the P3HT$^+$/PEDOT:PSS interface to the PEDOT:PSS layer is favorable, consistent with the effective hole collecting nature of the PEDOT:PSS layer in a P3HT:PCBM BHJ solar cell. This result also accounts for the significant enhancement in the electron-blocking and hole-transporting ability of PEDOT:PSS by depositing a thin layer of P3HT on top of PEDOT:PSS prior to the deposition of P3HT:PCBM blend, which in turn produces larger overlaps in LDOS below the Fermi levels of PEDOT:PSS and P3HT$^+$/PEDOT:PSS interface and a further improvement in power conversion efficiency.[40] Using the cross-sectional STM technique, we are able to explore the interfacial energy band diagrams and electronic structures across the P3HT:PCBM/PEDOT:PSS interfaces, which is important for further understanding the local carrier transport and collection behaviors of polymer solar cells. Figure 6 shows a summary

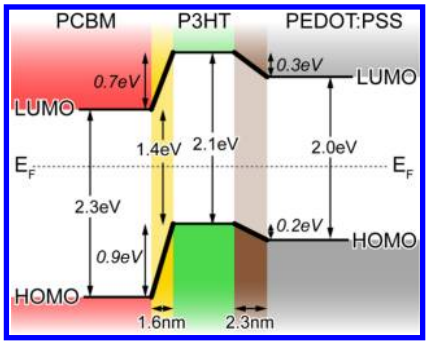

Figure 6. Schematic energy band diagrams for the device with a structure of PCBM/P3HT/PEDOT:PSS.

of the interfacial band diagrams consisting of band alignments and interfacial band widths at the interfaces between P3HT and PCBM and between PEDOT:PSS and P3HT:PCBM hybrid layers in a BHJ polymer solar revealed by the cross-sectional STM technique.[41−43]

In conclusion, this study demonstrates the direct visualization of interfacial band mapping images of an optimized P3HT/PCBM bulk heterojunction solar cell across the film thickness using cross-sectional scanning tunneling microscope (XSTM) with samples cleaved in situ in an ultrahigh vacuum (UHV) chamber. The unique advantage of using XSTM to characterize BHJ solar cells makes it possible to simultaneously explore the quantitative link between vertical morphologies and their local interfacial electronic properties at an atomic-scale resolution between the two opposite electrodes. Thus, this approach has great potential to become a useful tool for the characterization and optimization of nanoscale phase-separated organic hybrid photovoltaic blends for understanding the local carrier generation, transport, and collection.

■ ASSOCIATED CONTENT

Supporting Information

Additional information and figures. This material is available free of charge via the Internet at http://pubs.acs.org.

■ AUTHOR INFORMATION

Corresponding Author

*E-mail: (Y.-P.C.) ypchiu@mail.nsysu.edu.tw; (C.-W.C.) chunwei@ntu.edu.tw.

Notes

The authors declare no competing financial interest.

■ ACKNOWLEDGMENTS

The authors would like to thank the National Science Council of Taiwan for financially supporting this research under Contract No. NSC 101-2112-M-110-007 -MY2, NSC 100-2119-M-002-020, and 100-2628-M-002-013-MY3.

■ REFERENCES

(1) Yu, G.; Gao, J.; Hummelen, J. C.; Wudl, F.; Heeger, A. J. *Science* **1995**, *270*, 1789−1791.
(2) Shaheen, S. E.; Brabec, C. J.; Sariciftci, N. S.; Padinger, F.; Fromherz, T.; Hummelen, J. C. *Appl. Phys. Lett.* **2001**, *78*, 841−843.
(3) Delgado, J. L.; Bouit, P.-A.; Filippone, S.; Herranz, MÁ.; Martín, N. *Chem. Commun.* **2010**, *46*, 4853−4865.
(4) Reyes-Reyes, M.; Kim, K.; Carroll, D. L. *Appl. Phys. Lett.* **2005**, *87*, 083506.
(5) Li, G.; Shrotriya, V.; Huang, J.; Yao, Y.; Moriarty, T.; Emery, K.; Yang, Y. *Nat. Mater.* **2005**, *4*, 864−868.
(6) Chen, H. Y.; Hou, J.; Zhang, S.; Liang, Y.; Yang, G.; Yang, Y.; Yu, L.; Wu, Y.; Li, G. *Nat. Photonics* **2009**, *3*, 649−653.
(7) Friend, R. H.; Denton, G. J.; Halls, J. J. M.; Harrison, N. T.; Holmes, A. B.; Kohler, A.; Lux, A.; Moratti, S. C.; Pichler, K.; Tessler, N.; Towns, K.; Wittmann, H. F. *Solid State Commun.* **1997**, *102*, 249−258.
(8) Savenije, T. J.; Warman, J. M.; Goossens, A. *Chem. Phys. Lett.* **1998**, *287*, 148−153.
(9) Scully, S. R.; McGehee, M. D. *J. Appl. Phys.* **2006**, *100*, 034907.
(10) Groves, C.; Reid, O. G.; Ginger, D. S. *Acc. Chem. Res.* **2010**, *43*, 612−620.
(11) Dante, M.; Peet, J.; Nguyen, T.-Q. *J. Phys. Chem. C.* **2008**, *112*, 7241−7249.
(12) Spadafora, E. J.; Demadrille, R.; Ratier, B.; Grévin, B. *Nano Lett.* **2010**, *10*, 3337−3342.
(13) Li, G.; Yao, Y.; Yang, H.; Shrotriya, V.; Yang, G.; Yang, Y. *Adv. Funct. Mater.* **2007**, *17*, 1636−1644.
(14) Ma, W.; Yang, C.; Gong, X.; Lee, K.; Heeger, A. J. *Adv. Funct. Mater.* **2005**, *15*, 1617−1622.
(15) Hoppe, H.; Glatzel, T.; Niggemann, M.; Hinsch, A.; Lux-Steiner, M. C.; Sariciftci, N. S. *Nano Lett.* **2005**, *5*, 269−274.

(16) Maturová, K.; Janssen, R. A. J.; Kemerink, M. *ACS Nano* **2009**, *3*, 627−636.
(17) Grévin, B.; Rannou, P.; Payerne, R.; Pron, A.; Travers, J. P. *J. Chem. Phys.* **2003**, *118*, 7097−7102.
(18) Maturová, K.; Bavel, S. S.; van Wienk, M. M.; Janssen, R. A. J.; Kemerink, M. *Adv. Funct. Mater.* **2011**, *21*, 261−269.
(19) Alvarado, S. F.; Rieβ, W.; Seidler, P. F.; Strohriegl, P. *Phys. Rev. B* **1997**, *56*, 1269−1278.
(20) Rinaldi, R.; Cingolani, R.; Jones, K. M.; Baski, A. A.; Morkoc, H.; Carlo, A. D.; Widany, J.; Sala, F. D.; Lugli, P. *Phys. Rev. B* **2001**, *63*, 075311.
(21) Yang, X.; Loos, J.; Veenstra, S. C.; Verhees, W. J. H.; Wienk, M. M.; Kroon, J. M.; Michels, M. A. J.; Janssen, R. A. *Nano Lett.* **2005**, *5*, 579−583.
(22) Bavel, S. S. V.; Sourty, E.; With, G. D.; Loos, J. *Nano Lett.* **2009**, *9*, 507−513.
(23) Huang, B. C.; Chiu, Y. P.; Huang, P. C.; Wang, W. C.; Tra, V. T.; Yang, J. C.; He, Q.; Lin, J. Y.; Chang, C. S.; Chu, Y. H. *Phys. Rev. Lett.* **2012**, *109*, 246807.
(24) Chiu, Y. P.; Chen, B. C.; Huang, B. C.; Shih, M. C.; Tu, L. W. *Appl. Phys. Lett.* **2010**, *96*, 082107.
(25) Chiu, Y. P.; Huang, B. C.; Shih, M. C.; Shen, J. Y.; Chang, P.; Chang, C. S.; Huang, M. L.; Tsai, M.-H.; Hong, M.; Kwo, J. *Appl. Phys. Lett.* **2011**, *99*, 212101.
(26) Chiu, Y. P.; Chen, Y. T.; Huang, B. C.; Shih, M. C.; Yang, J. C.; He, Q.; Liang, C. W.; Seidel, J.; Chen, Y. C.; Ramesh, R.; Chu, Y. H. *Adv. Mater.* **2011**, *23*, 1530−1534.
(27) Improvements on the sample preparation for the cleavage process would not perturb the conductivity of organic samples significantly and could solve the challenges with the feedback loop in STM measurements.
(28) Contaminations on the surfaces could induce other electronic information of organic samples in experiments.
(29) Freenstra, R. M. *Phys. Rev. B* **1994**, *50*, 4561−4570.
(30) Herzing, A. A.; Richter, L. J.; Anderson, I. M. *J. Phys. Chem. C* **2010**, *114*, 17501−17508.
(31) Drummy, L. F.; Davis, R. J.; Moore, D. L.; Durstock, M.; Vaia, R. A.; Hsu, J. W. P. *Chem. Mater.* **2011**, *23*, 907−912.
(32) Bredas, J. L.; Cornil, J.; Heeger, A. J. *Adv. Mater.* **1996**, *8*, 447−452.
(33) Alvarado, S. F.; Seidler, P. F.; Lidzey, D. G.; Bradley, D. D. C. *Phys. Rev. Lett.* **1998**, *81*, 1082−1085.
(34) Brabec, C. J.; Cravino, A.; Meissner, D.; Sricifitci, N. S.; Formherz, T.; Rispens, M. T.; Sanchez, L.; Hummelen, J. C. *Adv. Funct. Mater.* **2001**, *11*, 374.
(35) Davis, R. J.; Lloyd, M. T.; Ferreira, S. R.; Bruzek, M. J.; Watkins, S. E.; Lindell, L.; Sehati, P.; Fahlman, M.; Anthony, J. E.; Hsu, J. W. P. *J. Mater. Chem.* **2011**, *21*, 1721−1729.
(36) Sariciftci, N. S.; Smilowitz, L.; Heeger, A. J.; Wudl, F. *Science* **1992**, *258*, 1474−1476.
(37) The partial miscibility of fullerene derivatives in a polymer matrix is commonly defined as a distinct mixed phase. The interfacial region could be regarded as a mixed phase region. Analyzing the electronic property at the interfacial region (or the mixed phase region) between $PCBM^+$ and $P3HT^+$ domains is around 60∼80% from PCBM. The observation from the STM measurement indicates the n-type electronic characteristic at the interfacial state.
(38) Kanai, Y.; Grossman, J. C. *Nano Lett.* **2007**, *7*, 1967−1972.
(39) Holst, J. J. M. V. D.; Uijttewaal, M. A.; Ramachandhran, B.; Coehoorn, R.; Bobbert, P. A. *Phys. Rev. B* **2009**, *79*, 085203.
(40) Liang, C. W.; Su, W. F.; Wang, L. *Appl. Phys. Lett.* **2009**, *95*, 133303.
(41) Guan, Z. L.; Kim, J. B.; Wang, H.; Jaye, C.; Fischer, D. A.; Loo, Y. L.; Kahn, A. *Org. Electron.* **2010**, *11*, 1779−1785.
(42) Davis, R. J.; Lloyd, M. T.; Ferreira, S. R.; Bruzek, M. J.; Watkins, S. E.; Lindell, L.; Sehati, P.; Fahlman, M.; Anthony, J. E.; Hsu, J. W. P. *J. Mater. Chem.* **2011**, *21*, 1721−1729.
(43) These offset in the HOMO or LUMO levels between $P3HT^+$ and $PCBM^+$ are smaller than the observations from Guan's[41], but more consistent to the results from Davis's.[42]